

Coupled Time-Dependent Proton Acceleration and Leptonic-Hadronic Radiation in Turbulent Supermassive Black Hole Coronae

Chengchao Yuan^{1,*}, Damiano F. G. Fiorillo¹, Maria Petropoulou², and Qinrui Liu^{3,4,5}

¹*Deutsches Elektronen-Synchrotron DESY, Platanenallee 6, 15738 Zeuthen, Germany*

²*Department of Physics, National and Kapodistrian University of Athens, University Campus Zografos, GR 15784, Athens, Greece*

³*Department of Physics, Engineering Physics and Astronomy, Queen's University, Kingston ON K7L 3N6, Canada*

⁴*Arthur B. McDonald Canadian Astroparticle Physics Research Institute, Kingston ON K7L 3N6, Canada and*

⁵*Perimeter Institute for Theoretical Physics, Waterloo ON N2L 2Y5, Canada*

(Dated: August 12, 2025)

Turbulent coronae of supermassive black holes can accelerate non-thermal particles to high energies and produce observable radiation, but capturing this process is challenging due to comparable timescales of acceleration, cooling, and the development of cascades. We present a time-dependent numerical framework that self-consistently couples proton acceleration—modeled by the Fokker-Planck equation—with leptonic-hadronic radiation. For the neutrino-emitting Seyfert galaxy NGC 1068, we reproduce the neutrino spectrum observed by IceCube, while satisfying gamma-ray constraints. We also consider a transient corona scenario, potentially emerging in non-jetted tidal disruption events like AT 2019dsg, and show that early-stage cascade feedback can impact proton acceleration and radiation processes in weaker coronae, producing delayed optical/ultraviolet, X-ray, and neutrino emissions of $\mathcal{O}(100\text{ d})$. This flexible code efficiently models multi-messenger signals from both steady and transient astrophysical sources, providing insights in combining particle acceleration and radiation mechanisms.

The recent detection of high-energy neutrinos from the nearby Seyfert galaxy NGC 1068 by IceCube [1, 2] provides compelling evidence for particle acceleration in active galactic nuclei (AGN). The neutrino spectrum, which peaks around 1–100 TeV, suggests a coronal origin [3–6] where protons could be accelerated by magnetized turbulence [3, 7, 8] or magnetic reconnection [5, 9–11] near the supermassive black hole (SMBH), and the gamma-rays are absorbed to satisfy the gamma-ray constraints [12–14]. These protons interact with ambient thermal protons and X-ray and optical/ultraviolet (OUV) photon fields to produce neutrinos and electromagnetic (EM) cascades making the sources obscured to high-energy gamma-rays [3, 5, 15, 16]. IceCube has found neutrino emission excess from additional X-ray bright Seyfert galaxies using a disk-corona model [17, 18]. A self-consistent model is generally needed to incorporate EM cascade feedback on proton cooling in the compact coronal regions.

Besides AGN coronae, which we consider to have achieved a steady state despite possible long-term variability [19–22], tidal disruption events (TDEs), in which the bound debris of destroyed stars powers a year-long transient spanning a broad electromagnetic spectrum [23], offer a unique laboratory to study particle acceleration in evolving coronae likely formed during the super-Eddington accretion phase [24]. Meanwhile, observed OUV and X-ray light curves (e.g., Refs. [25, 26]) provide critical constraints.

Modeling the coronal emission, especially from transients, generally requires coupling time-dependent proton acceleration with radiative feedback across multi-

ple spatial and temporal scales. So we provide, for the first time, a systematic description that couples them together, within a Fokker-Planck realization of acceleration (e.g., Refs. [27–30]); we validate our time-dependent code by applying it to a steady environment that is crucial for multi-messenger astrophysics, namely the NGC 1068 corona, and then we prove its power by applying to a time-dependent setup for TDE transient coronae. Applying to NGC 1068 reproduces the observed neutrino spectrum while satisfying gamma-ray constraints, as an expansion upon Ref. [7] where cascade emission was not calculated. For TDEs such as AT 2019dsg [31], we propose a phenomenological approach linking the time-dependent mass accretion rate onto the SMBH with transient corona properties. By evolving the system from the peak accretion time to approximately 450 days afterward, we demonstrate how early-stage cascade feedback shapes delayed multiwavelength and neutrino emission.

Another key motivation is to provide the community with a versatile and efficient tool well suited for multi-messenger modeling of a wide range of astrophysical transients (e.g., gamma-ray bursts, AGN flares) and steady sources, accommodating diverse acceleration mechanisms such as turbulence (e.g., Ref. [32]), magnetic reconnection (e.g., Refs. [33–35]), shearing flows (e.g., Refs. [36, 37]), and shock acceleration (e.g., Refs. [38–40]).

TURBULENT PROTON ACCELERATION

We model proton acceleration by magnetized turbulence within a corona, which refers to a spherical region

of radius R_{co} around a SMBH, permeated by a magnetic field of strength B , and containing thermal protons and electrons with densities n_p and n_e , respectively. Considering an SMBH of mass $M = 10^7 M_7 M_\odot$, we define the radius parameter $\mathcal{R} = R_{\text{co}}/r_g$ in terms of the gravitational radius $r_g = GM/c^2 \simeq 1.5 \times 10^{12} M_7 \text{ cm}$. Given the typical opacity $\tau_T \sim 0.1 - 1$ [41], we infer the electron density $n_e = \tau_T/(\sigma_T R_{\text{co}})$. For a steady corona in the core of an AGN, such as NGC 1068, we fix $\tau_T = 0.5$ and assume $n_p \approx n_e \simeq 2.5 \times 10^{10} M_7^{-1} (\mathcal{R}/20)^{-1} \text{ cm}^{-3}$ (as in Refs. [3, 7]). Given the magnetization σ_B of the plasma, the magnetic field strength can be parameterized as $B = \sqrt{4\pi\sigma_B n_p m_p c^2}$, where m_p is the proton mass.

Inside magnetized coronae, particles can be accelerated via plasma turbulence or magnetic reconnection. In this work, we focus on the turbulent acceleration scenario with $\mathcal{R} = 20$ and $\sigma_B = 0.1$. The strength of the turbulent magnetic field fluctuations can be written as $\sigma_{\text{tur}} = \sigma_B (\delta B/B)^2$, where δB is the root-mean-squared value of the turbulent magnetic field. The typical scale of turbulent structures is described by the coherent length $l_{\text{cl}} = \eta_{\text{cl}} R_{\text{co}} \lesssim R_{\text{co}}$, where η_{cl} is the fractional scale.

Using l_{cl} and the diffusion coefficient in momentum space $D_p \sim 0.1 \sigma_{\text{tur}} p^2 c / l_{\text{cl}}$, derived from particle-in-cell simulations [42] as a function of proton momentum p , we write the energy-independent proton acceleration time as

$$t_{\text{acc}} \equiv \frac{p^2}{D_p} = \frac{10 l_{\text{cl}}}{\sigma_{\text{tur}} c} \simeq 10^4 M_7 \left(\frac{\mathcal{R}}{20} \right) \left(\frac{\eta_{\text{cl}}}{\sigma_{\text{tur}}} \right) \text{ s}. \quad (1)$$

We then solve the time-dependent Fokker–Planck (FP) equations describing second-order Fermi acceleration, which accounts for the feedback of cascade photons on proton cooling initiated by $\gamma\gamma$ pair production and hadronic processes including photopion ($p\gamma$) interaction, proton-proton (pp) collision, Bethe–Heitler (BH) pair production, and proton synchrotron ($p\text{-sy}$) radiation. These processes are simulated using the open-source AM³ [43] software for time-dependent modeling of leptonic-hadronic interactions, where the cooling timescale can be retrieved as $t_{\text{cool}} = (t_{p\gamma}^{-1} + t_{pp}^{-1} + t_{\text{BH}}^{-1} + t_{p\text{-sy}}^{-1})^{-1}$, and is used as an input to the FP equation. Regarding the proton escape timescale (t_{esc}), the proton mean free path is determined by the coherent length of turbulent magnetic field fluctuations and the proton gyro-radius $l_r = E_p/(eB)$, where the proton energy is $E_p = pc$. This can be expressed as $\lambda_{\text{mfp}} = l_{\text{cl}}(l_r/l_{\text{cl}})^\zeta$, with $\zeta > 0$. The exact value of ζ depends on the turbulence intermittency, and simulations suggest $0.3 < \zeta < 0.5$ [44, 45]. We adopt $\zeta = 1/3$ as a fiducial value. The escape time, inspired by random walk arguments, is then $t_{\text{esc}} = R_{\text{co}}^2/(\lambda_{\text{mfp}} c)$, with a lower limit of R_{co}/c .

Given the acceleration time t_{acc} , cooling time t_{cool} , and escape time t_{esc} , the time-dependent FP equation can be efficiently and stably solved using a tridiagonal matrix approach with the Chang–Cooper scheme [27] to properly account for momentum flow. A detailed description

of the numerical methods and a test case verifying the convergence of time-dependent solutions to the steady-state solution are presented in the supplemental material (SM). This numerical framework self-consistently couples proton acceleration (via the FP equation) with the time-dependent cooling time obtained from AM³, which includes feedback from EM cascades. The acceleration of secondary pairs is neglected because cooling dominates over acceleration. The spectra of EM cascades and neutrinos are computed directly by AM³, whereas the proton spectra are obtained from solving the FP equation. Importantly, we find that the accelerated proton spectra are largely insensitive to the injection term $q(p) = dN_p/(dtdVd^3p)$ in the momentum space, especially in the high-energy regime. Therefore, in applications to NGC 1068 and transient corona of TDE AT 2019dsg, we adopt $q(p) \propto p \exp(-p/p_{\text{inj}})$ with $p_{\text{inj}} = 10 m_p c$, which yields an accurate proton distribution for $E_p > p_{\text{inj}} c \sim 10 \text{ GeV}$.

STEADY CORONA IN NGC 1068

The nearby Seyfert galaxy NGC 1068 (luminosity distance $d_L \simeq 10.1 \text{ Mpc}$ [47]) provides an exceptional case study for probing proton acceleration and hadronic processes in a steady corona, as its $\sim 1\text{--}100 \text{ TeV}$ neutrino spectrum, combined with faint gamma-ray emission, favors a coronal origin. In this scenario, $p\gamma$ interactions with dense X-ray photons dominate neutrino production, while efficient $\gamma\gamma$ attenuation explains the low gamma-ray flux at $E_\gamma \gtrsim 0.1 \text{ GeV}$.

We apply the coupled time-dependent proton acceleration by magnetized turbulence to reproduce the neutrino spectrum and study the associated EM cascade. For a magnetically powered corona, the proton luminosity is constrained by the dissipation of turbulent magnetic energy. We approximate the dissipation timescale as the magnetic reconnection time scale $t_{\text{diss}} \approx Bl_{\text{cl}}/(\epsilon_{\text{rec}} v_A \delta B)$ [42, 48], where $v_A = c\sqrt{\sigma_B/(1+\sigma_B)}$ is the Alfvén speed and $\epsilon_{\text{rec}} \sim 0.1$ defines the reconnection rate, e.g., $\epsilon_{\text{rec}} v_A \delta B$ [49, 50]. The proton acceleration power is then parameterized as a fraction ϵ_p of the turbulent magnetic energy dissipation rate L_B within the corona of volume $V_{\text{co}} = 4\pi R_{\text{co}}^3/3$,

$$L_p = \epsilon_p L_B = \frac{\epsilon_p}{t_{\text{diss}}} \frac{(\delta B)^2}{8\pi} V_{\text{co}}, \quad (2)$$

which is used to normalize the accelerated proton spectra. In the following calculations, we fix $\mathcal{R} = 20$, $\sigma_B = \sigma_{\text{tur}} = 0.1$, and assume $\delta B/B \sim 1$. In contrast, η_{cl} and ϵ_p are varied, e.g., $\epsilon_p, \eta_{\text{cl}} \leq 1$, since they determine the maximum proton energy $E_{p,\text{max}}$ through t_{acc} and the flux levels of neutrinos and EM cascades, respectively.

We consider isotropized OUV and coronal X-ray photons as $p\gamma$ targets. The external photon injection rates

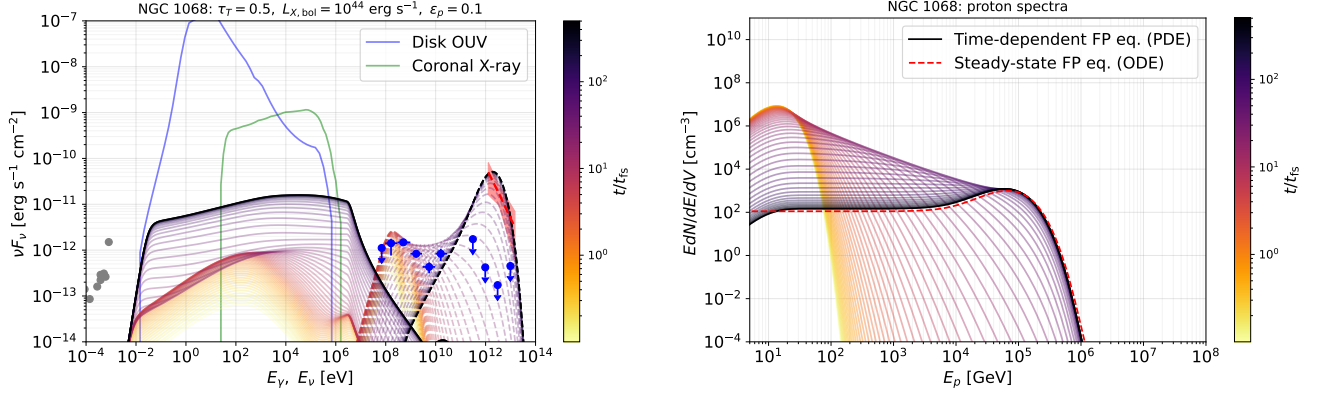


FIG. 1. NGC 1068: Observed all-flavor neutrino (dashed) and EM cascade (solid) spectra (left panel), and in-source proton density spectra (right panel) at times ranging from $0.1t_{fs} = 0.1R_{co}/c$ to $500t_{fs}$. Radio [46], gamma-ray [12, 13], and neutrino [2] observations are shown as gray points, blue points, and the red-shaded area. The green and blue curves respectively show the coronal X-ray and OUV spectra. The solid curves in the right panel show the proton spectra from time dependent FP equation, whereas the dashed red curve denotes the steady-state solution from the reduced ordinary differential equation (ODE).

to AM^3 , $\dot{n}_i(E_\gamma) \equiv E_\gamma d^2 n_i / (dE_\gamma dt)$ with $i = \text{OUV or X}$, are inferred from the luminosity distributions dL_i/dE_γ via $\dot{n}_i = (dL_i/dE_\gamma)/V_i$, where $V_{\text{OUV}} = 4\pi R_{\text{OUV}}^3/3$ and $V_X = V_{co}$. OUV photons primarily originate from the accretion disk and the radius $R_{\text{OUV}} \gtrsim 10R_{co}$ is estimated using the multi-temperature disk profile as $R_{\text{OUV}} \approx [3GML_{\text{OUV}}/(8\pi\eta_{\text{rad}}c^2\sigma_S T^4)]^{1/3}$, with $L_{\text{OUV}} = \int dE_\gamma (dL_{\text{OUV}}/dE_\gamma)$, radiation efficiency $\eta_{\text{rad}} \sim 0.1$, disk temperature T , and Stefan-Boltzmann constant σ_S . For NGC 1068, the blue curve in Fig. 1 shows the OUV spectrum (retrieved from Refs. [7, 51]) with peak temperature of $T \simeq 4 \times 10^4$ K and $L_{X,\text{bol}} = \int dE_\gamma (dL_X/dE_\gamma) \sim 10^{44}$ erg s $^{-1}$ [7]. We ignore the contribution from infrared photons [52], since they are produced in a further extended region. We use the coronal X-ray spectra from Ref. [3], normalized to $L_{X,\text{bol}}$ (green curve). Proton cooling and hadronic emissions from BH pair productions, proton synchrotron, and pp collisions are also included, with n_p as the target proton density which is much larger than the density of accelerated protons.

With this configuration, the left panel of Fig. 1 illustrates the coevolution of neutrino (dashed) and EM cascade (solid) spectra from $0.1t_{fs}$ to $500t_{fs}$, where $t_{fs} = R_{co}/c$ represents the free escaping timescale for photons and neutrinos. Using $\epsilon_p = 0.1$ and $\sigma_{\text{tur}} = 0.3$, the neutrino and EM spectra converges efficiently to the steady state at $t \sim 300t_{fs}$ (equivalent to $\sim 10t_{\text{acc}}$), which reproduces the neutrino observations without exceeding the gamma-ray upper limits, since the GeV gamma-rays observed by Fermi-LAT [53] would be produced in a different, extended region [54–61]. The early-time ($t \lesssim 5t_{fs}$) low-energy neutrino spectra are driven by pp interactions of low-energy protons, whereas pp and BH processes jointly dominate the EM cascades. As the maximum proton energy $E_{p,\text{max}}$ increases (as shown in the right panel

of Fig. 1), $p\gamma$ interactions dominate neutrino production, and EM cascades generate broader EM spectra. In particular, coronal X-ray photons efficiently deplete gamma-rays above 10^7 eV via $\gamma\gamma$ attenuation, with the resulting electron/positron (e^\pm) pairs reprocessing the energy into lower-energy radiation down to ~ 0.01 eV. The contributions of various radiation processes to the cascade spectra are shown in Fig. 5 in SM. The cascade spectra closely resemble those expected from reconnection scenarios (e.g., Refs. [10, 11]), making them ineffective discriminators of the proton acceleration mechanism in the corona.

To verify the time-dependent treatment, we compare the time-dependent proton spectra (solid curves) with the steady-state solution (red dashed) obtained from the reduced FP equation in the right panel. Even with a low initial injection peak (e.g., 10 GeV), protons are stably accelerated to 40–100 TeV, consistent with the predicted value from balancing the acceleration and cooling rates (see Fig. 5 in SM). The deviation from the steady-state solution, which neglects cascade emissions, is negligible, as coronal X-ray photons dominate proton cooling.

TRANSIENT TDE CORONA

The previous application to NGC 1068 demonstrates the effectiveness of combining FP proton acceleration with radiation processes. We now take a step further to investigate, in the coupled acceleration-cascade framework, the time-dependent signatures of TDEs. Although the dynamics and physical properties of SMBH coronae remain uncertain, we develop a phenomenological model for TDE coronae by assuming a transient corona powered by a TDE with a characteristic mass fallback rate $\propto t^{-5/3}$. We adopt AT 2019dsg as a prototype, as it is a well-identified TDE with multi-wavelength light

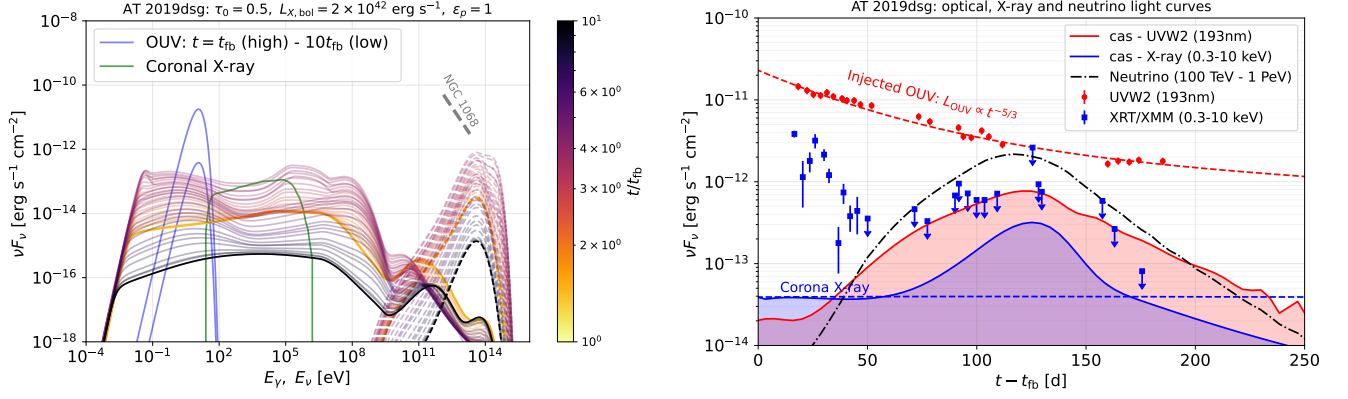


FIG. 2. Left panel: Same as the left panel of Fig. 1, but for the transient corona of the TDE AT 2019dsg. The time is scaled to the TDE mass fallback time $t_{fb} \simeq 45$ d, up to $10t_{fb}$. Right panel: Coronal cascade optical/UV (solid red), X-ray (solid blue), and neutrino (dash-dotted black) light curves of TDE AT 2019dsg. The injected OUV and X-ray light curves are shown as dashed lines. Red and blue points represent the UV (193 nm) [31] and X-ray (0.3–10 keV) [62] observations, respectively.

curve measurements in the radio, infrared, OUV, and X-ray bands [31, 63]. Basic properties of AT 2019dsg are as follows [31, 62, 63]: redshift $z = 0.051$ (luminosity distance $d_L \simeq 228.3$ Mpc), SMBH mass $M \sim 5 \times 10^6$ – $10^7 M_\odot$, and a peak bolometric OUV luminosity $L_{OUV,pk} \simeq 10^{44}$ erg s $^{-1}$ characterized by a blackbody spectrum with temperature $k_B T_{OUV} \sim 3.4$ eV, where k_B is the Boltzmann constant.

Using these parameters, the typical mass fallback time can be estimated as $t_{fb} \simeq 3.9 \times 10^6 M_7 (M_*/M_\odot)^{-1/10}$ s, where $M_* \sim 0.5 - 2 M_\odot$ [64, 65] is the mass of the disrupted star. After t_{fb} , the OUV luminosity and mass accretion rate onto the SMBH for $t > t_{fb}$ can be described respectively as $L_{OUV}(t) = L_{OUV,pk} (t/t_{fb})^{-5/3}$, as illustrated by the red dashed curve in Fig. 2 (right panel), and

$$\dot{M} = \frac{\eta_{acc} M_*}{3 t_{fb} c^2} \left(\frac{t}{t_{fb}} \right)^{-5/3}, \quad (3)$$

where $\eta_{acc} \sim 0.01 - 0.1$ [24, 66, 67] denotes the fraction of gravitationally bound stellar mass that is ultimately accreted, and \dot{M} is normalized by $\int \dot{M} dt = \eta_{acc} M_*/2$, as roughly half of the disrupted star’s mass remains bound.

Since the coronal protons may originate from accreted material, we take $n_p \propto \dot{M}$ as a reasonable approximation. Consequently, the Thomson opacity $\tau_T = n_p \sigma_T R_{co}$ evolves as $\tau_T = \tau_0 \min[1, \dot{M}/\dot{M}_{Edd}]$, where $\dot{M}_{Edd} = L_{Edd}/(\eta_{rad} c^2)$ is the Eddington accretion rate, $L_{Edd} \simeq 1.3 \times 10^{46} M_7$ erg s $^{-1}$ is the Eddington luminosity, and $\tau_0 \sim 0.1$ – 1 represents the opacity in the super-Eddington phase. We keep R_{co} fixed, since the expansion of R_{co} would render the corona unstable and cause it to quickly merge with the extended disk winds. Given the same $\sigma_B = \sigma_{tur} = 0.1$, $\tau_0 = 0.5$, and $\eta_{cl} = 0.3$ as used for NGC 1068, we obtain the proton luminosity at t_{fb} , $L_p(t_{fb}) = 2.2 \times 10^{43} \epsilon_p$ erg s $^{-1}$.

The X-ray emissions from TDE coronae are typically faint compared to NGC 1068. For AT 2019dsg, the X-ray observations [62] (see the blue points in the right panel of Fig. 2) imply a coronal luminosity of $L_{X,bol} \lesssim 2 \times 10^{42}$ erg s $^{-1}$ in the 0.1–100 keV range (similar to Refs. [64, 68], where constant X-ray light curves are assumed). The initial fast decaying X-ray light curve could be caused by accretion disk cooling [62]. In addition, thermal OUV photons produced at the blackbody radius $R_{OUV} \sim \sqrt{L_{OUV}/(4\pi\sigma_S T_{OUV}^4)}$ also contribute to proton cooling. The blue and green curves in the left panel of Fig. 2 show the spectra of the OUV with fixed T_{OUV} and AGN-like coronal X-ray target photons, where R_{OUV} and R_{co} are used to infer the photon injection rates to AM 3 .

Applying the transient corona model, we evolve proton acceleration and radiation processes from t_{fb} to $10t_{fb}$. We adopt optimistic values $\eta_{acc} = 0.1$ and $\epsilon_p = 1$ to maximize coronal multiwavelength and neutrino emissions. The left panel of Fig. 2 shows the resulting neutrino (dashed) and EM cascade (solid) spectra. The faint coronal X-ray emission leads to a higher $E_{p,max}$ due to a lower $p\gamma$ cooling rate (see Fig. 6 and the right-bottom panel of Fig. 5 in SM), causing the neutrino spectrum to peak at $E_\nu \sim 100$ TeV. The EM cascades dominate proton cooling above 1 PeV, and they also enhance the cooling rates in the 1 TeV – 1 PeV range by a factor of ~ 2 .

Interestingly, delayed OUV and X-ray cascade emissions are expected, as shown in the right panel of Fig. 2. This feature mainly arises from early-stage EM cascade feedback. In the $p\gamma$ -efficient limit, where $f_{p\gamma} = t_{p\gamma}^{-1}/(t_{cool}^{-1} + t_{esc}^{-1}) \rightarrow 1$, the initial cascade luminosity $L_{cas} \sim (5/8)L_p$ exceeds the coronal X-ray luminosity. The buildup of EM cascades, together with the accumulation of protons during the super-Eddington phase and for $t < t_{esc}$ (see Fig. 6 in SM), jointly drive the multi-wavelength light curves to peak at $t \simeq 140$ d, consistent

with the spectra in the left panel of Fig. 2 and with the OUV (193 nm, red solid) and X-ray (0.3–10 keV, blue solid) light curves in the right panel.

A similar interpretation applies to the neutrino light curve (0.1–1 PeV, black dash-dotted). The coronal neutrino peak flux and its time delay relative to the OUV peak (~ 140 d) are comparable to those of the isotropic radiation zone extending to the dust torus [64, 68], but the coronal neutrinos peak at lower energies (~ 100 TeV), offering a new perspective for interpreting the potential neutrino–TDE correlations [31, 63, 69–72], especially the time delays of $\mathcal{O}(100$ d). For a decaying $L_{X,\text{bol}} \propto t^{-5/3}$, $E_{p,\text{max}}$ would increase over time and the light curves are expected to decline faster after the peak, following $f_{p\gamma} L_p \propto L_{X,\text{bol}} L_p \propto t^{-10/3}$. One caveat is that the OUV, X-ray and neutrino cascade light curves in the right panel represent upper limits for AT 2019dsg, since in reality—especially in the weak corona case—lower values of $\tau_0 \lesssim 0.5$ and $\epsilon_p \lesssim 1$ are expected. In such cases, a correction factor of $\sim 2\tau_0\epsilon_p$ should be applied to the neutrino and EM cascade fluxes.

SUMMARY AND DISCUSSION

We developed an efficient and stable numerical code to solve the Fokker-Planck equations describing proton accelerations and combined proton acceleration due to magnetized turbulence in coronae with leptonic-hadronic radiation modeling in a fully time-dependent manner. This framework has been applied to self-consistently model the neutrino and EM cascade spectra from a steady-state and a transient/dynamic corona, motivated by NGC 1068 and TDE. In the former case, the power densities of accelerated protons and EM cascades are lower than those of the injected X-ray and OUV target photon fields. We find that radiation feedback onto the accelerated proton distribution is negligible, and the solution converges perfectly to a steady state that reproduces the neutrino spectra while being consistent with gamma-ray observations and upper limits. For TDEs, where the X-ray emission from the corona is typically weak, EM cascade feedback can be more important (see the test case and Fig. 4 in SM). We propose a transient corona scenario with time-dependent proton injection power, magnetic field strength, and target proton and photon densities, which predicts delayed OUV, X-ray, and neutrino emissions due to the dominant early-stage EM cascade feedback for the prototype AT 2019dsg.

The steady corona model can be directly applied to other neutrino-emitting Seyfert galaxies, such as NGC 4151, NGC 3079 [73], NGC 7469 [74], and the Circinus galaxy [75], whereas the transient corona model is testable via multi-messenger observations of TDEs, especially for subpopulations with potential neutrino correlations or strong non-jetted X-ray emissions, as the coronal

contribution would be prominent.

Beyond turbulent acceleration and SMBH coronae, this coupled acceleration–cascade framework has broader applications, though it does not yet capture anisotropic particle distributions. Its flexible timescales and injection terms enable modeling of other mechanisms such as magnetic reconnection, shear flow acceleration, and shock acceleration. The time-dependent feature suits both steady sources and transient multi-messenger phenomena, e.g., gamma-ray bursts, TDEs, AGN flares, and microquasars, when extended to include lepton acceleration.

Leveraging the efficient leptonic-hadronic modeling software AM³, we find a way to overcome the challenge of reconciling the tiny time steps in compact acceleration regions with long-term system evolution. This method bridges plasma dynamics and acceleration microphysics—addressed respectively by magnetohydrodynamic simulations (e.g., Refs. [76–78]) and particle-in-cell simulations (e.g., Refs. [42, 77, 79, 80])—with radiation modeling to improve the interpretation and prediction of high-energy astrophysical phenomena.

Acknowledgments – We thank Martin Lemoine for useful discussions during ICRC2025. This work has been partially funded by the “Program for the Promotion of Exchanges and Scientific Collaboration between Greece and Germany IKYDA–DAAD” 2024 (IKY project ID 309; DAAD project ID: 57729829). M.P. acknowledges support from the Hellenic Foundation for Research and Innovation (H.F.R.I.) under the “2nd call for H.F.R.I. Research Projects to support Faculty members and Researchers” through the project UNTRAPHOB (Project ID 3013).

* chengchao.yuan@desy.de

- [1] M. G. Aartsen *et al.* (IceCube), *Phys. Rev. Lett.* **124**, 051103 (2020), [arXiv:1910.08488](https://arxiv.org/abs/1910.08488) [astro-ph.HE].
- [2] R. Abbasi *et al.* (IceCube), *Science* **378**, 538 (2022), [arXiv:2211.09972](https://arxiv.org/abs/2211.09972) [astro-ph.HE].
- [3] K. Murase, S. S. Kimura, and P. Meszaros, *Phys. Rev. Lett.* **125**, 011101 (2020), [arXiv:1904.04226](https://arxiv.org/abs/1904.04226) [astro-ph.HE].
- [4] Y. Inoue, D. Khangulyan, and A. Doi, *Astrophys. J. Lett.* **891**, L33 (2020), [arXiv:1909.02239](https://arxiv.org/abs/1909.02239) [astro-ph.HE].
- [5] A. Kheirandish, K. Murase, and S. S. Kimura, *Astrophys. J.* **922**, 45 (2021), [arXiv:2102.04475](https://arxiv.org/abs/2102.04475) [astro-ph.HE].
- [6] P. Padovani *et al.*, *Nature Astron.* **8**, 1077 (2024), [arXiv:2405.20146](https://arxiv.org/abs/2405.20146) [astro-ph.HE].
- [7] D. F. G. Fiorillo, L. Comisso, E. Peretti, M. Petropoulou, and L. Sironi, *Astrophys. J.* **974**, 75 (2024), [arXiv:2407.01678](https://arxiv.org/abs/2407.01678) [astro-ph.HE].
- [8] L. Saurenhuis, F. Capel, F. Oikonomou, and J. Buchner, (2025), [arXiv:2507.06110](https://arxiv.org/abs/2507.06110) [astro-ph.HE].
- [9] R. Mbarek, A. Philippov, A. Chernoglazov, A. Levinson, and R. Mushotzky, *Phys. Rev. D* **109**, L101306 (2024), [arXiv:2310.15222](https://arxiv.org/abs/2310.15222) [astro-ph.HE].
- [10] D. F. G. Fiorillo, M. Petropoulou, L. Comisso,

- E. Peretti, and L. Sironi, *Astrophys. J.* **961**, L14 (2024), [arXiv:2310.18254 \[astro-ph.HE\]](#).
- [11] D. Karavola, M. Petropoulou, D. F. G. Fiorillo, L. Comisso, and L. Sironi, *JCAP* **04**, 075, [arXiv:2410.12638 \[astro-ph.HE\]](#).
- [12] S. Abdollahi *et al.* (Fermi-LAT), *Astrophys. J. Suppl.* **247**, 33 (2020), [arXiv:1902.10045 \[astro-ph.HE\]](#).
- [13] V. A. Acciari *et al.* (MAGIC), *Astrophys. J.* **883**, 135 (2019), [arXiv:1906.10954 \[astro-ph.HE\]](#).
- [14] M. Ajello, K. Murase, and A. McDaniel, *Astrophys. J. Lett.* **954**, L49 (2023), [arXiv:2307.02333 \[astro-ph.HE\]](#).
- [15] K. Fang, J. S. Gallagher, and F. Halzen, *Astrophys. J.* **933**, 190 (2022), [arXiv:2205.03740 \[astro-ph.HE\]](#).
- [16] K. Fang, E. L. Rodriguez, F. Halzen, and J. S. Gallagher, *Astrophys. J.* **956**, 8 (2023), [arXiv:2307.07121 \[astro-ph.HE\]](#).
- [17] R. Abbasi *et al.* (IceCube), *Astrophys. J.* **988**, 141 (2025), [arXiv:2406.07601 \[astro-ph.HE\]](#).
- [18] S. Yu *et al.* (IceCube), *PoS ICRC2023*, 1533 (2024), [arXiv:2307.15620 \[astro-ph.HE\]](#).
- [19] F. Ursini *et al.*, *Astron. Astrophys.* **577**, A38 (2015), [arXiv:1501.03426 \[astro-ph.HE\]](#).
- [20] D. R. Wilkins, *Astronomische Nachrichten* **337**, 557 (2016).
- [21] A. Jana *et al.*, *Astron. Astrophys.* **699**, A62 (2025), [arXiv:2505.13242 \[astro-ph.GA\]](#).
- [22] S. Laha, C. Ricci, J. C. Mather, E. Behar, L. C. Gallo, F. Marin, R. Mbarek, and A. Hankla, *Front. Astron. Space Sci.* **11**, 1530392 (2024), [arXiv:2412.11321 \[astro-ph.HE\]](#).
- [23] M. J. Rees, *Nature* **333**, 523 (1988).
- [24] K. Murase, S. S. Kimura, B. T. Zhang, F. Oikonomou, and M. Petropoulou, *Astrophys. J.* **902**, 108 (2020), [arXiv:2005.08937 \[astro-ph.HE\]](#).
- [25] K. Auchettl, J. Guillochon, and E. Ramirez-Ruiz, *Astrophys. J.* **838**, 149 (2017), [arXiv:1611.02291 \[astro-ph.HE\]](#).
- [26] S. van Velzen *et al.*, *Astrophys. J.* **908**, 4 (2021), [arXiv:2001.01409 \[astro-ph.HE\]](#).
- [27] J. S. Chang and G. Cooper, *Journal of Computational Physics* **6**, 1 (1970).
- [28] B. T. Park and V. Petrosian, *Astrophysical Journal Supplement Series* **103**, 255 (1996).
- [29] P. A. Becker, T. Le, and C. D. Dermer, *Astrophys. J.* **647**, 539 (2006), [arXiv:astro-ph/0604504](#).
- [30] L. Stawarz and V. Petrosian, *Astrophys. J.* **681**, 1725 (2008), [arXiv:0803.0989 \[astro-ph\]](#).
- [31] R. Stein *et al.*, *Nature Astron.* **5**, 510 (2021), [arXiv:2005.05340 \[astro-ph.HE\]](#).
- [32] V. Petrosian, *Space Sci. Rev.* **173**, 535 (2012), [arXiv:1205.2136 \[astro-ph.HE\]](#).
- [33] E. G. Zweibel and M. Yamada, *Annual Review of Astronomy and Astrophysics* **47**, 291 (2009).
- [34] A. Lazarian, L. Vlahos, G. Kowal, H. Yan, A. Beresnyak, and E. M. de Gouveia Dal Pino, *Space Sci. Rev.* **173**, 557 (2012), [arXiv:1211.0008 \[astro-ph.SR\]](#).
- [35] L. Sironi, D. A. Uzdensky, and D. Giannios, *arXiv e-prints*, [arXiv:2506.02101 \(2025\)](#), [arXiv:2506.02101 \[astro-ph.HE\]](#).
- [36] F. M. Rieger, *Galaxies* **7**, 78 (2019), [arXiv:1909.07237 \[astro-ph.HE\]](#).
- [37] S. S. Kimura, K. Murase, and B. T. Zhang, *Phys. Rev. D* **97**, 023026 (2018), [arXiv:1705.05027 \[astro-ph.HE\]](#).
- [38] L. O. Drury, *Rept. Prog. Phys.* **46**, 973 (1983).
- [39] R. D. Blandford and D. Eichler, *Physics Reports* **154**, 1 (1987).
- [40] M. Weidinger and F. Spanier, *Astron. Astrophys.* **573**, A7 (2015), [arXiv:1410.5380 \[astro-ph.HE\]](#).
- [41] C. Ricci *et al.*, *Mon. Not. Roy. Astron. Soc.* **480**, 1819 (2018), [arXiv:1809.04076 \[astro-ph.HE\]](#).
- [42] L. Comisso and L. Sironi, *Astrophys. J.* **886**, 122 (2019), [arXiv:1909.01420 \[astro-ph.HE\]](#).
- [43] M. Klinger, A. Rudolph, X. Rodrigues, C. Yuan, G. F. de Clairfontaine, A. Fedynitch, W. Winter, M. Pohl, and S. Gao, *Astrophys. J. Suppl.* **275**, 4 (2024), [arXiv:2312.13371 \[astro-ph.HE\]](#).
- [44] M. Lemoine, *J. Plasma Phys.* **89**, 175890501 (2023), [arXiv:2304.03023 \[physics.plasm-ph\]](#).
- [45] P. Kempster, D. B. Fielding, E. Quataert, A. K. Galishnikova, M. W. Kunz, A. A. Philippov, and B. Ripperda, *Mon. Not. Roy. Astron. Soc.* **525**, 4985 (2023), [arXiv:2304.12335 \[astro-ph.HE\]](#).
- [46] Y.-L. Chang, C. Brandt, and P. Giommi, *Astron. Comput.* **30**, 100350 (2020), [arXiv:1909.11455 \[astro-ph.HE\]](#).
- [47] R. B. Tully, E. J. Shaya, I. D. Karachentsev, H. M. Courtois, D. D. Kocevski, L. Rizzi, and A. Peel, *Astrophys. J.* **676**, 184 (2008), [arXiv:0705.4139 \[astro-ph\]](#).
- [48] L. Comisso, *Astrophys. J.* **972**, 9 (2024), [arXiv:2405.18227 \[astro-ph.HE\]](#).
- [49] L. Comisso and A. Bhattacharjee, *J. Plasma Phys.* **82**, 595820601 (2016), [arXiv:1609.02998 \[physics.plasm-ph\]](#).
- [50] P. A. Cassak, Y. H. Liu, and M. A. Shay, *J. Plasma Phys.* **83**, 715830501 (2017), [arXiv:1708.03449 \[physics.plasm-ph\]](#).
- [51] A. Marconi, G. Risaliti, R. Gilli, L. K. Hunt, R. Maiolino, and M. Salvati, *Mon. Not. Roy. Astron. Soc.* **351**, 169 (2004), [arXiv:astro-ph/0311619](#).
- [52] J. R. Mullaney, D. M. Alexander, A. D. Goulding, and R. C. Hickox, *Mon. Not. Roy. Astron. Soc.* **414**, 1082 (2011), [arXiv:1102.1425 \[astro-ph.CO\]](#).
- [53] A. A. Abdo *et al.* (Fermi-LAT), *Astrophys. J. Suppl.* **188**, 405 (2010), [arXiv:1002.2280 \[astro-ph.HE\]](#).
- [54] J.-P. Lenain, C. Ricci, M. Turler, D. Dorner, and R. Walter, *Astron. Astrophys.* **524**, A72 (2010), [arXiv:1008.5164 \[astro-ph.CO\]](#).
- [55] T. M. Yoast-Hull, J. S. G. III, E. G. Zweibel, and J. E. Everett, *Astrophys. J.* **780**, 137 (2014), [arXiv:1311.5586 \[astro-ph.HE\]](#).
- [56] A. Ambrosone, M. Chianese, D. F. G. Fiorillo, A. Marinelli, and G. Miele, *Astrophys. J. Lett.* **919**, L32 (2021), [arXiv:2106.13248 \[astro-ph.HE\]](#).
- [57] B. Eichmann, F. Oikonomou, S. Salvatore, R.-J. Dettmar, and J. Becker Tjus, *Astrophys. J.* **939**, 43 (2022), [arXiv:2207.00102 \[astro-ph.HE\]](#).
- [58] A. Lamastra, F. Fiore, D. Guetta, L. A. Antonelli, S. Colafrancesco, N. Menci, S. Puccetti, A. Stamerra, and L. Zappacosta, *Astron. Astrophys.* **596**, A68 (2016), [arXiv:1609.09664 \[astro-ph.HE\]](#).
- [59] S. Inoue, M. Cerruti, K. Murase, and R.-Y. Liu, *PoS ICRC2023*, 1161 (2023), [arXiv:2207.02097 \[astro-ph.HE\]](#).
- [60] E. Peretti, A. Lamastra, F. G. Saturni, M. Ahlers, P. Blasi, G. Morlino, and P. Cristofari, *Mon. Not. Roy. Astron. Soc.* **526**, 181 (2023), [arXiv:2301.13689 \[astro-ph.HE\]](#).
- [61] K. Yasuda, N. Sakai, Y. Inoue, and A. Kusenko, *Phys. Rev. Lett.* **134**, 151005 (2025), [arXiv:2405.05247 \[astro-ph.HE\]](#).

- [62] G. Cannizzaro *et al.*, *Mon. Not. Roy. Astron. Soc.* **504**, 792 (2021), [arXiv:2012.10195 \[astro-ph.HE\]](#).
- [63] S. van Velzen *et al.*, *Mon. Not. Roy. Astron. Soc.* **529**, 2559 (2024), [arXiv:2111.09391 \[astro-ph.HE\]](#).
- [64] W. Winter and C. Lunardini, *Astrophys. J.* **948**, 42 (2023), [arXiv:2205.11538 \[astro-ph.HE\]](#).
- [65] P. Mohan, T. An, Y. Zhang, J. Yang, X. Yang, and A. Wang, *Astrophys. J.* **927**, 74 (2022), [arXiv:2106.15799 \[astro-ph.HE\]](#).
- [66] C. Yuan, B. T. Zhang, W. Winter, and K. Murase, *Astrophys. J.* **974**, 162 (2024), [arXiv:2406.11513 \[astro-ph.HE\]](#).
- [67] C. Yuan, W. Winter, B. T. Zhang, K. Murase, and B. Zhang, *Astrophys. J.* **982**, 196 (2025), [arXiv:2411.07925 \[astro-ph.HE\]](#).
- [68] C. Yuan and W. Winter, *Astrophys. J.* **956**, 30 (2023), [arXiv:2306.15659 \[astro-ph.HE\]](#).
- [69] S. Reusch *et al.*, *Phys. Rev. Lett.* **128**, 221101 (2022), [arXiv:2111.09390 \[astro-ph.HE\]](#).
- [70] N. Jiang, Z. Zhou, J. Zhu, Y. Wang, and T. Wang, *Astrophys. J. Lett.* **953**, L12 (2023), [arXiv:2307.16667 \[astro-ph.HE\]](#).
- [71] C. Yuan, W. Winter, and C. Lunardini, *Astrophys. J.* **969**, 136 (2024), [arXiv:2401.09320 \[astro-ph.HE\]](#).
- [72] R.-L. Li, C. Yuan, H.-N. He, Y. Wang, B.-Y. Zhu, Y.-F. Liang, N. Jiang, and D.-M. Wei, (2024), [arXiv:2411.06440 \[astro-ph.HE\]](#).
- [73] A. Neronov, D. Savchenko, and D. V. Semikoz, *Phys. Rev. Lett.* **132**, 101002 (2024), [arXiv:2306.09018 \[astro-ph.HE\]](#).
- [74] G. Sommani, A. Franckowiak, M. Lincetto, and R.-J. Dettmar, *Astrophys. J.* **981**, 103 (2025), [arXiv:2403.03752 \[astro-ph.HE\]](#).
- [75] K. Murase, C. M. Karwin, S. S. Kimura, M. Ajello, and S. Buson, *Astrophys. J. Lett.* **961**, L34 (2024), [arXiv:2312.16089 \[astro-ph.HE\]](#).
- [76] M. Lemoine, *Phys. Rev. D* **104**, 063020 (2021), [arXiv:2104.08199 \[astro-ph.HE\]](#).
- [77] V. Bresci, M. Lemoine, L. Gremillet, L. Comisso, L. Sironi, and C. Demidem, *Phys. Rev. D* **106**, 023028 (2022), [arXiv:2206.08380 \[astro-ph.HE\]](#).
- [78] D. J. Price *et al.*, *Publ. Astron. Soc. Austral.* **35**, 31 (2018), [arXiv:1702.03930 \[astro-ph.IM\]](#).
- [79] K. Wong, V. Zhdankin, D. A. Uzdensky, G. R. Werner, and M. C. Begelman, *Astrophys. J. Lett.* **893**, L7 (2020), [arXiv:1901.03439 \[astro-ph.HE\]](#).
- [80] V. Zhdankin, D. A. Uzdensky, G. R. Werner, and M. C. Begelman, *Mon. Not. Roy. Astron. Soc.* **493**, 603 (2020), [arXiv:1908.08032 \[astro-ph.HE\]](#).
- [81] J. Crank and P. Nicolson, *Mathematical Proceedings of the Cambridge Philosophical Society* **43**, 50 (1947).
- [82] V. S. Berezinsky and A. Y. Smirnov, *Astrophys. Space Sci.* **32**, 461 (1975).

SUPPLEMENTAL MATERIAL

Numerical methods for solving Fokker-Planck equations coupled with leptonic-hadronic radiation

We present a stable numerical method for solving the time-dependent Fokker-Planck (FP) equation that describes proton acceleration in momentum space,

$$\frac{\partial f}{\partial t} = \frac{1}{p^2} \frac{\partial}{\partial p} \left[p^2 D_p(p) \frac{\partial f}{\partial p} + \frac{p^3}{t_{\text{cool}}} f \right] - \frac{f}{t_{\text{esc}}} + q(p), \quad (4)$$

where $f(p, t) = \frac{dN_p}{dp^3 dV dt}$ is particle distribution and $q(p) = \frac{dN_p}{dp^3 dV dt}$ is the proton injection rate. The momentum diffusion term D_p is related to the acceleration timescale as $D_p = p^2/t_{\text{acc}}$. To solve the partial differential equation (PDE), we adopt linear and logarithmic discretizations for the time t and the momentum p , respectively, with $t_n = t_0 + n\Delta t$ (for $n = 1, 2, \dots$) and $p_i = p_0 (p_{\text{max}}/p_0)^{i/N}$ (for $i = 0, 1, \dots, N$). The minimum and maximum proton momenta are set to $p_0 = 5m_p c$ and $p_{\text{max}} = 10^{11}m_p c$ to meet the requirements of most cases. A proton momentum grid with $N = 274$, corresponding to 25 bins per energy decade, is used to improve numerical stability. To simplify the presentation below, we define $\dot{p} \equiv p/t_{\text{cool}} > 0$ as the momentum advection term and adopt the following notations

- $f_i^n \equiv f(p_i, t_n)$, $D_i \equiv D_p(p_i)$, $\dot{p}_i \equiv \dot{p}(p_i)$, $q_i \equiv q(p_i)$, $\lambda_i \equiv 1/t_{\text{esc}}(p_i)$
- $x_{i+1/2} = (x_i + x_{i+1})/2$, $\Delta x_{i+1/2} = x_{i+1} - x_i$, $\Delta x_i = (x_{i+1} - x_{i-1})/2$ for $x = D_p$, p and \dot{p} . For instance, $p_{i+1/2} = (p_i + p_{i+1})/2$.

The flux term $\Phi(p, t) \equiv D_p(p) \frac{\partial f}{\partial p} + \dot{p} f$ could be discretized as

$$\Phi_{i+1/2}^n = D_{i+1/2} \frac{f_{i+1}^n - f_i^n}{\Delta p_{i+1/2}} + \dot{p}_{i+1/2} [(1 - \delta) f_{i+1}^n + \delta f_i^n],$$

where $0 \leq \delta \leq 1$ is the Chang-Cooper weighting factor [27] defined as

$$\delta = \frac{1}{w} - \frac{1}{e^w - 1}$$

with $w = \Delta p_{i+1/2} \dot{p}_{i+1/2} / D_{i+1/2}$. This method ensures both the preservation of positivity and the correct equilibrium solution, even in strongly cooling-dominated ($w \gg 1$) regimes. In practice, we find that $w \gg 1$, especially at high p , where proton cooling dominates the spectral evolution and the resulting $\delta \rightarrow 0$, corresponding to the upwinding scheme. The physical meaning is that when the cooling rate is exceedingly high, protons flow from high p_{i+1} to low p_i .

We then have the expression for $\partial f / \partial t$ at p_i and t_n ,

$$\frac{\partial f}{\partial t} \Big|_{i,n} \approx \frac{1}{p_i^2 \Delta p_i} \left[p_{i+1/2}^2 \Phi_{i+1/2}^n - p_{i-1/2}^2 \Phi_{i-1/2}^n \right] - f_i^n \lambda_i + q_i.$$

The time evolution of f_i is then computed using the Crank–Nicolson time discretization scheme [81], e.g.,

$$\frac{f_i^{n+1} - f_i^n}{\Delta t} = \frac{1}{2} \left[\frac{\partial f}{\partial t} \Big|_{i,n+1} + \frac{\partial f}{\partial t} \Big|_{i,n} \right].$$

This implicit scheme is stable for linear problems while maintaining second-order accuracy in time, and it can be expressed in a tridiagonal matrix form as

$$A_i f_{i-1}^{n+1} + B_i f_i^{n+1} + C_i f_{i+1}^{n+1} = R_i^n.$$

Defining the coefficients

$$\begin{aligned} a_i &= \frac{p_{i+1/2}^2 D_{i+1/2}}{p_i^2 \Delta p_i \Delta p_{i+1/2}}, \quad b_i = \frac{p_{i+1/2}^2 \dot{p}_{i+1/2}}{p_i^2 \Delta p_i}, \\ c_i &= \frac{p_{i-1/2}^2 D_{i-1/2}}{p_i^2 \Delta p_i \Delta p_{i-1/2}}, \quad d_i = \frac{p_{i-1/2}^2 \dot{p}_{i-1/2}}{p_i^2 \Delta p_i}, \end{aligned} \quad (5)$$

we explicitly write down

$$\begin{aligned} A_i &= -\frac{\Delta t}{2} (c_i - \delta d_i), \\ B_i &= 1 + \frac{\Delta t}{2} [a_i - \delta b_i + c_i + (1 - \delta) d_i + \lambda_i], \\ C_i &= -\frac{\Delta t}{2} [a_i + (1 - \delta) b_i], \\ R_i^n &= \left(1 - \frac{\lambda_i \Delta t}{2} \right) f_i^n + \frac{\Delta t}{2} \{ a_i (f_{i+1}^n - f_i^n) \\ &\quad + b_i [(1 - \delta) f_{i+1}^n + \delta f_i^n] - c_i (f_i^n - f_{i-1}^n) \\ &\quad - d_i [(1 - \delta) f_i^n + \delta f_{i-1}^n] + 2q_i \}. \end{aligned}$$

The system can efficiently evolve from t_n to t_{n+1} by applying the inverse of a tridiagonal matrix \mathcal{M} ,

$$(\vec{f}_i^{n+1})^T = \mathcal{M}^{-1} \cdot (\vec{R}_i^n)^T, \quad (6)$$

where $\vec{f}_i^{n+1} = (f_0^{n+1}, \dots, f_N^{n+1})$, $\vec{R}_i^n = (R_0^n, \dots, R_N^n)$, and \mathcal{M} can be explicitly written as

$$\mathcal{M} = \begin{bmatrix} B_0 & C_0 & 0 & 0 & \cdots & 0 \\ A_1 & B_1 & C_1 & 0 & \cdots & 0 \\ \vdots & \ddots & \ddots & \ddots & \ddots & \vdots \\ 0 & \cdots & 0 & A_{N-1} & B_{N-1} & C_{N-1} \\ 0 & \cdots & 0 & 0 & A_N & B_N \end{bmatrix}. \quad (7)$$

By repeating the above procedure K times and updating the input terms accordingly, the proton distribution at time $t_K = t_0 + K\Delta t$ can be obtained.

Coupling to AM³ – So far, we have developed a numerical method for solving the time-dependent FP equation. The implementation of the Chang-Cooper method and a reasonable Δt significantly improve stability. For the AGN and TDE corona case, $\Delta t \sim 0.001 R_{\text{co}}/c$ would be sufficient. To couple the FP equation with AM³ [43], an open-source software for time-dependent leptonic-hadronic radiation modeling, which works with the proton density distribution $n_p(E, t) = Ed^2 N_p / (dEdV) =$

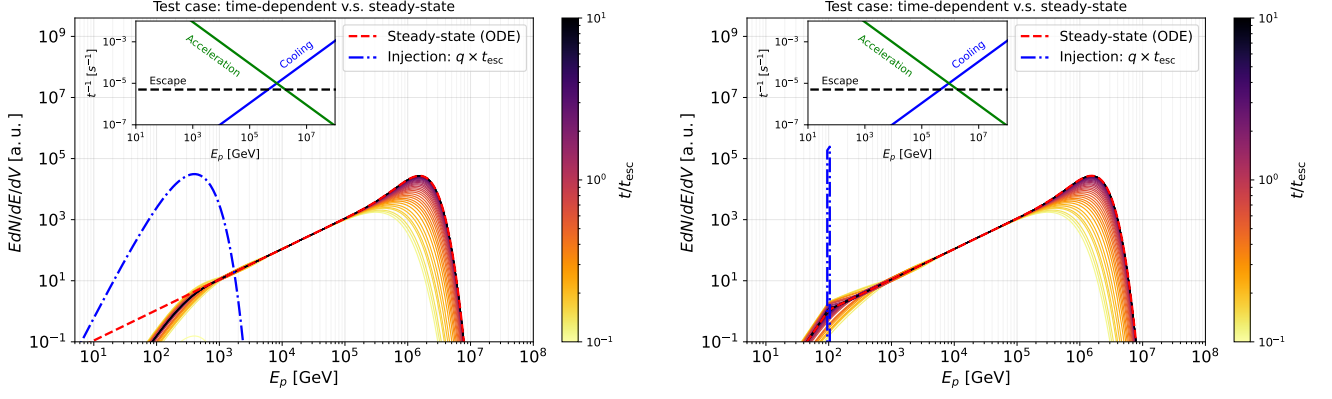


FIG. 3. Test of numerical solutions to FP equations: comparison between time-dependent solutions (solid curves) and steady-state solutions (red dashed curve), normalized to arbitrary units. The injection rates (blue dash-dotted curve) are also shown. The insets display the proton escape, acceleration, and cooling rates. Different injection functions $q \propto p \exp(-p/p_{\text{inj}})$ and $q \propto \delta(p - p_{\text{inj}})$ with $p_{\text{inj}} = 10^2 m_p c$ are used respectively in the left and right panels.

$4\pi p^3 f(p, t)|_{E=p_c}$, we normalize $f(p, t)$ using the proton power L_p and the volume of the acceleration zones V ,

$$L_p = -4\pi cV \int p^2 D_p(p) \frac{\partial f}{\partial p} dp. \quad (8)$$

One critical point is that, to avoid repeated proton cooling, we use AM³ solely to self-consistently evolve the distributions of photons, neutrinos, and other secondary particles such as e^\pm , μ^\pm , π^\pm , and π^0 produced by $p\gamma$, pp , $\gamma\gamma$, proton synchrotron (p-syn) and Bethe-Heitler (BH) interactions. The evolution of the proton spectra is determined exclusively by the FP equation, which already incorporates escape and cooling processes. Accordingly, after each time step, we update $n_p(E, t)$ in AM³, and retrieve the overall, real-time cooling timescale from AM³ to the FP solver, e.g., $t_{\text{cool}} = (t_{pp}^{-1} + t_{p\gamma}^{-1} + t_{\text{BH}}^{-1} + t_{\text{p-syn}}^{-1})^{-1}$, where pp , $p\gamma$, BH, and proton synchrotron cooling rates are included. Depending on the dynamics of the accelerator, the injection rate q , acceleration time t_{acc} , and escape time t_{esc} can take arbitrary forms and be time-dependent.

Steady-state solution – To test the stability and convergence of the solutions to the time-dependent FP equation, it is useful to solve Eq. 4 in the steady state by setting $\partial f / \partial t = 0$. The PDE then reduces to an ordinary differential equation (ODE), which can also be expressed in tridiagonal matrix form, for example,

$$\alpha_i f_{i-1} + \beta_i f_i + \gamma_i f_{i+1} = r_i,$$

with the coefficients

$$\begin{aligned} \alpha_i &= c_i - \delta d_i, \\ \beta_i &= -a_i + \delta b_i - c_i - (1 - \delta) d_i - \lambda_i, \\ \gamma_i &= a_i + (1 - \delta) b_i, \\ r_i &= -q_i. \end{aligned}$$

We impose a zero-flux boundary condition at p_0 , i.e., $\Phi(p_0) = 0$, and an absorption boundary condition at p_{max} , i.e., $f(p_N) = 0$:

$$D_{1/2} \frac{f_1 - f_0}{\Delta p_{1/2}} + \dot{p}_{1/2} [(1 - \delta) f_1 + \delta f_0] = 0, \quad f_N = 0.$$

While solving this ODE, we found that the Chang–Cooper method remains effective in controlling the momentum flow direction.

Test cases – To verify the robustness of the numerical methods presented above, we design a simple test case featuring free escape, shock acceleration with $t_{\text{acc}} \propto p$, and synchrotron cooling with $t_{\text{cool}} \propto p^{-1}$. We select a constant escape time and time-independent acceleration and cooling rates, given by

$$t_{\text{esc}} = 2 \times 10^5 \text{ s}, \quad t_{\text{acc}} = 10^6 \left(\frac{p}{p_c} \right) \text{ s}, \quad t_{\text{cool}} = 10^4 \left(\frac{p}{p_c} \right)^{-1} \text{ s},$$

where $p_c = 10^7 m_p c$ is a characteristic proton momentum. All other processes are switched off, and no feedback effects on the radiation field are considered.

Fig. 3 summarizes the results of the test case. The solid curves in color represent the proton distributions obtained from the time-dependent FP equation at times ranging from $0.1 t_{\text{esc}}$ to $10 t_{\text{esc}}$. The red dashed curve shows the steady-state solution. To verify the independence of q , the injection rates $q(p) \propto p \exp(-p/p_{\text{inj}})$ and $q(p) \propto \delta(p - p_{\text{inj}})$, with $p_{\text{inj}} = 10^2 m_p c$, are respectively used in the left and right panels. By comparing the time-dependent solutions with the steady-state solutions, we summarize the following conclusions:

- The time-dependent solution obtained from solving the complete FP equation (PDE) converges efficiently and stably to the steady-state solution derived from the reduced ODE.

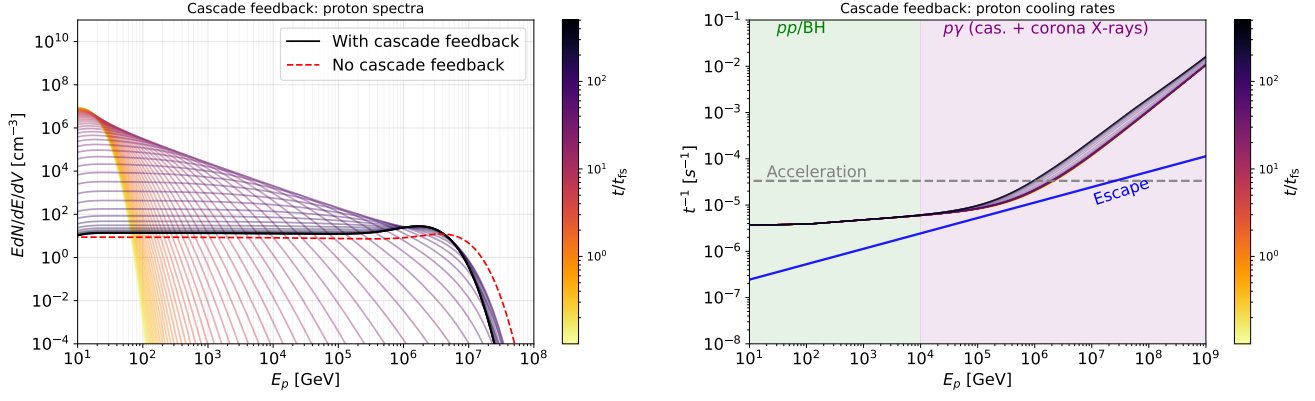


FIG. 4. Test of the impact of the EM cascade for a corona with weaker X-ray luminosity (e.g., $L_{X,\text{bol}} < L_p$). NGC 1068's corona is used as an example, with parameters identical to those in the main paper except for a lower luminosity of $L_{X,\text{bol}} = 5 \times 10^{41} \text{ erg s}^{-1}$. Left panel: Proton spectra obtained with EM cascade feedback (solid curves) and without cascade feedback (red solid curve). Right panel: Proton cooling rates at times from $0.1t_{\text{fs}} = 0.1R_{\text{co}}/c$ to $500t_{\text{fs}}$, including the contribution from cascade photons. The acceleration and escape rates are also shown. The green and purple areas represent the regimes where pp/BH and $p\gamma$ processes, respectively, dominate proton cooling.

- The proton distribution for $p > p_{\text{inj}}$ is independent of the shape of the injection function q in the time-dependent treatment.
- The maximum energy of accelerated protons is consistent with the energy determined by the balance condition $t_{\text{acc}}^{-1} = t_{\text{cool}}^{-1}$ (see the insets of Fig. 3).

In more complex scenarios, particularly when L_p is comparable to or higher than the injection power of external photons, feedback to the radiation field via electromagnetic cascades induced by hadronic processes increases the cooling rates. The resulting additional photons enhance the $p\gamma$ and BH interactions, which can reduce the peak energy of accelerated protons.

Fig. 4 shows the proton spectra (left panel) and cooling rates (right panel) for this case, using NGC 1068 as an example. All physical setups and parameters are the same as in the main paper, except that a lower coronal X-ray luminosity of $L_{X,\text{bol}} = 5 \times 10^{41} \text{ erg s}^{-1} < L_p \simeq 4 \times 10^{42} \text{ erg s}^{-1}$ is used. The results demonstrate that the EM cascade could enhance the proton cooling rate by a factor of

$$f_{\text{cas}} \sim \max \left[1, \frac{5f_{p\gamma}L_p}{8CL_{X,\text{bol}}} \right],$$

where $f_{p\gamma} = t_{p\gamma}^{-1}/(t_{\text{cool}}^{-1} + t_{\text{esc}}^{-1})$ is the $p\gamma$ efficiency at $E_{p,\text{max}}$ and the correction factor $\mathcal{C} \sim 2-3$ accounts for the difference in the widths of the cascade and coronal X-ray spectra. Consequently, the proton maximum energy shifts to lower energies.

Regarding code efficiency, the time-dependent FP solver is fast, typically converging to a steady state within

one minute if EM cascade feedback from AM³ is turned off. Most of the computational power is devoted to the leptonic-hadronic modeling by AM³, especially in compact coronae, which requires very small time steps.

EM cascade spectra, proton cooling rates and TDE proton spectra

Here, we present the components of the electromagnetic (EM) cascade spectra and the proton cooling rates for NGC 1068 (upper panels of Fig. 5) and the tidal disruption event (TDE) AT 2019dsg (bottom panels of Fig. 5) to support the interpretation of the EM cascade, neutrino, and proton spectra discussed in the main paper. The time evolution of proton spectra in TDE corona is also shown in Fig. 6. The main conclusions drawn from these figures are summarized below:

- In compact coronae, the late-stage EM spectra are universally dominated by e^\pm pairs produced via $\gamma\gamma$ attenuation (see e.g., Refs. [15, 82]), as the protons are accelerated to high energies, while in the early stage, EM cascades from pp and BH processes could dominate (e.g., NGC 1068).
- The maximum proton energy approaches the value determined by $t_{\text{acc}}^{-1} = t_{\text{cool}}^{-1}$.
- For AT 2019dsg, the buildup of EM cascades and accelerated protons during the super-Eddington phase (i.e., $\dot{M} > \dot{M}_{\text{Edd}}$) and for $t < t_{\text{esc}}$ jointly drive the peaks of the multiwavelength and neutrino light curves.

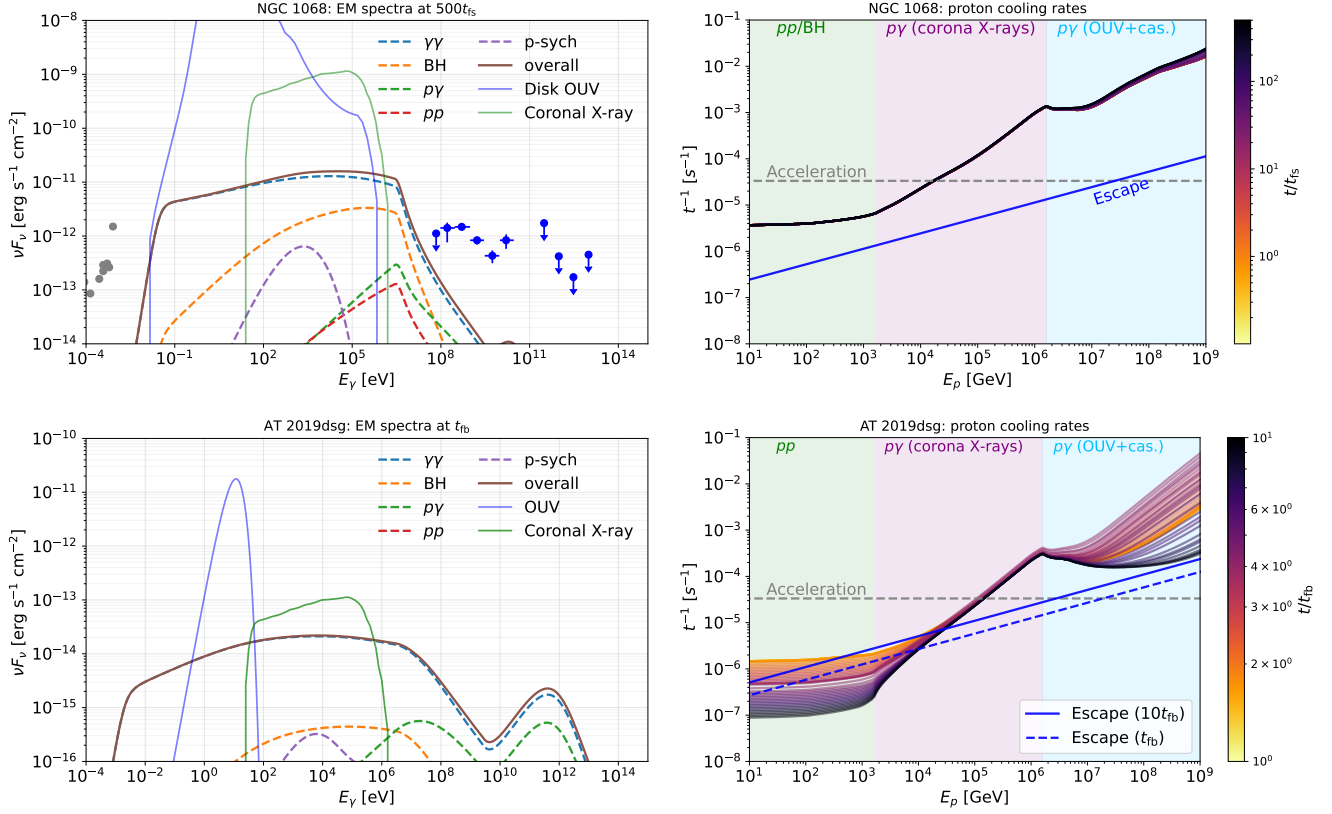


FIG. 5. Left panels: EM cascade spectral components, including contributions from $\gamma\gamma$ /BH pairs, leptons from $p\gamma$ / pp interactions, and proton synchrotron radiation, are shown for NGC 1068 (upper panel) at $500t_{fs}$ and for the TDE AT 2019dsg (bottom panel) at t_{fb} , where $t_{fs} = R_{co}/c$ is the free escaping rate and t_{fb} is the TDE mass fallback time. The radio and X-ray observations of NGC 1068 are shown as the gray and blue points. The OUV and coronal X-ray spectra are also shown. Both calculations account for $\gamma\gamma$ attenuation by the extragalactic background light. Right panels: Proton cooling rates at various times are shown, with colors ranging from yellow to black. The horizontal dashed gray curve represents the acceleration rate, while the blue lines depict the proton escape rates. The shaded regions from left to right indicate proton cooling dominated by pp /BH interactions, by $p\gamma$ interactions with coronal X-ray photons, and by interactions with OUV and cascade photons.

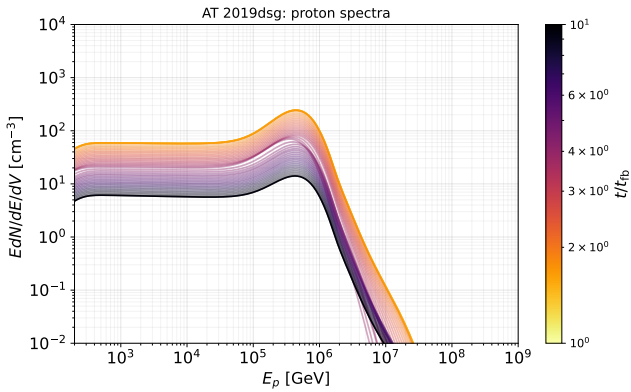


FIG. 6. TDE AT 2019dsg: in-source proton density spectra at times ranging from t_{fb} to $10t_{fb}$.